Geochemistry, Geophysics, Geosystems®

AGU ADVANCING EARTH AND SPACE SCIENCE

RESEARCH ARTICLE
10.1029/2022GC010338

Authigenic Clays Versus Carbonate Formation as Products of Marine Silicate Weathering in the Input Sequence to the Sumatra Subduction Zone

M. E. Torres[1], K. L. Milliken[2], A. Hüpers[3], J.-H. Kim[4], and S.-G. Lee[5]

[1]College Earth Ocean and Atmospheric Science, Oregon State University, Corvallis, OR, USA, [2]Bureau of Economic Geology, University of Texas at Austin, Austin, TX, USA, [3]MARUM-Center for Marine Environmental Sciences, University of Bremen, Bremen, Germany, [4]Petroleum & Marine Division, Korea Institute of Geoscience and Mineral Resources, Daejeon, South Korea, [5]Geology Division, Korea Institute of Geoscience and Mineral Resources, Daejeon, South Korea

Key Points:

- Continent-derived minerals shed from the Himalayas undergo weathering in anoxic sequences of the Nicobar Fan
- Co-occurring peaks of dissolved radiogenic strontium and methane support coupling of silicate weathering and methanogenesis
- Silicates in the early fan are replaced by carbonate; geochemical data in the later-stage fan point to formation of authigenic clays

Supporting Information:

Supporting Information may be found in the online version of this article.

Correspondence to:

M. E. Torres,
marta.torres@oregonstate.edu

Citation:

Torres, M. E., Milliken, K. L., Hüpers, A., Kim, J.-H., & Lee, S.-G. (2022). Authigenic clays versus carbonate formation as products of marine silicate weathering in the input sequence to the Sumatra subduction zone. *Geochemistry, Geophysics, Geosystems*, *23*, e2022GC010338. https://doi.org/10.1029/2022GC010338

Received 12 JAN 2022
Accepted 17 MAR 2022

Author Contributions:

Conceptualization: M. E. Torres, K. L. Milliken
Funding acquisition: M. E. Torres, K. L. Milliken, A. Hüpers
Investigation: M. E. Torres, K. L. Milliken, A. Hüpers, J.-H. Kim, S.-G. Lee
Methodology: M. E. Torres, K. L. Milliken
Project Administration: M. E. Torres, K. L. Milliken
Resources: M. E. Torres, K. L. Milliken

Abstract We use geochemical and petrographic data from anoxic sequences of the Nicobar Fan to document extensive marine silicate weathering (MSiW) in the input sediment of the Sumatra subduction zone and the conditions that result in authigenic minerals originating from this reaction: precipitation of authigenic carbonate—which sequesters carbon—and formation of authigenic clay—which releases CO_2. Increase in $^{87}Sr/^{86}Sr$ in pore fluids from International Ocean Discovery Program Expedition 362 (Site U1480 to 0.71376 and Site U1481 to 0.71296) reveals a radiogenic strontium contribution from alteration of the Himalayan continental sediment that dominates the Nicobar Fan. Peaks in the dissolved strontium isotope data coincide with zones of methane presence, consistent with MSiW reactions driven by CO_2 generation during methanogenesis. Later-stage fan sequences from 24 to 400 mbsf (meters below seafloor) contain only minor carbonate with $^{87}Sr/^{86}Sr$ ratios that deviate only slightly from the co-eval seawater values (0.70920–0.70930); geochemical data in this zone point to a contribution of authigenic clay formation. In contrast, microscopy and elemental mapping of the carbonate-cemented zones in the earliest fan deposits (>780 mbsf) show replacement of feldspars and dense minerals by carbonate, which ranges in volume from a few percent of the grain to near total grain obliteration. This deeper authigenic carbonate is significantly enriched in radiogenic ^{87}Sr (0.71136–0.71328). Thus, MSiW leads to distinct products, likely in response to a weathering-derived supply of silica in the younger setting versus calcium enrichment via diffusion from oceanic basement in the older sequence.

Plain Language Summary Unstable minerals in sediments shed from the continents continue to undergo weathering in the early stages of burial, which is more pronounced in zones where methane generation increases the sediment acidity. Materials derived from dissolution of continent-derived silicates may appear as newly formed (authigenic) silicates (mostly clay minerals) and also contribute to the nucleation and composition of authigenic carbonates. The authigenic mineral reactions documented here in the input sediments of the Sumatra subduction zone provide constraints on global elemental budgets and the characteristics of materials before they are subducted.

1. Introduction

As reviewed in Torres et al. (2020), CO_2 generated during methanogenesis near continental margins induces weathering of reactive silicate phases that promote carbonate formation, following the net reaction shown in Equation 1. This general reaction consumes CO_2, increases alkalinity, and can sequester carbon at global rates similar to estimates associated with alteration of oceanic crust (Torres et al., 2020). Similar, and even more massive, processes of silicate weathering and sequestration of CO_2 in authigenic carbonate have also been documented in the deeper subsurface of several basins (Hutcheon & Abercrombie, 1990; Hutcheon et al., 1993; Land & Macpherson, 1992; Lu et al., 2011; Milliken, 2004; Milliken & Land, 1991; Smith & Ehrenberg, 1989), providing evidence for the global significance of this reaction.

$$\text{Cation} - \text{rich silicates} + 2CO_2 + 3H_2O \rightarrow H_4SiO_4 + 2HCO_3^- + Ca^{2+} + \text{other dissolved cations} \quad (1)$$

A sink for the silica, cations and alkalinity released from weathering dissolution of unstable silicates is the formation of marine authigenic clays, which releases CO_2, as indicated in Equation 2.

Supervision: M. E. Torres, K. L. Milliken, J.-H. Kim
Writing – original draft: M. E. Torres, K. L. Milliken
Writing – review & editing: A. Hüpers, J.-H. Kim

$$H_4SiO_4 + Al(OH)_3 + \left(Mg^{2+},\ K^{+},\ Na^{+}\right) + HCO_3^{-} \rightarrow \text{new clay mineral} + CO_2 + H_2O \quad (2)$$

Authigenic clay formation is highly dependent on silica availability. Dunlea et al. (2017) documents the significance of authigenic clay formation in the oxic sediment of the South Pacific Gyre and shows how changes in distribution and rates of biogenic silica burial over the Cenozoic, translated to a reduction in the extent of reverse weathering that influenced atmospheric CO_2 levels and drove global cooling over the past 50 million years.

The conditions that result in either authigenic clay or carbonate formation are still not fully understood. Recent drilling offshore Sumatra (International Ocean Discovery Program [IODP] Expedition 362; McNeill, Dugan, & Petronotis, 2017) captured deposition of the Bengal–Nicobar fan system composed of deep-water siliciclastic sediments (McNeill, Dugan, & Petronotis, 2017). Using geochemical and petrographic data we show that the earlier fan deposits were influenced by ongoing basement alteration that supplied dissolved calcium and consumed magnesium; a cation balance that promoted formation of carbonate cements via carbon-silica reaction networks (Equation 1). In the most recent fan sediment, the formation of authigenic carbonate is less evident; rather, our geochemical data point to the formation of authigenic clay minerals, fueled in part by dissolved silica supplied from biogenic opal and ash in the most recent (<2 Ma) post fan sediments (Equation 2). We further explored the relative roles of carbonate formation via the traditionally studied carbon cycling pathways versus the coupled silicate-carbonate system and investigate the role of these cements on the compactional state of the formation. Our results are of relevance because (a) the reaction products (authigenic clay vs. carbonate) either release or sequester CO_2, with climate implications; (b) authigenic carbonate formation may impact the amount of carbon trapped in the downgoing slab, affecting the overall carbon cycling in the arc; and (c) formation of cements within a sediment section impact the mechanical and hydrogeologic properties of the formation.

2. Sites U1480 and U1481 Offshore Sumatra

The incoming sequence to the Sumatra subduction zone includes a 4–5 km thick Bengal-Nicobar fan at the trench. These input sequences were drilled ∼225 km seaward of the deformation front during IODP Expedition 362 (McNeill, Dugan, & Petronotis, 2017). Site U1480 recovered input sediment to ∼1,420 mbsf (meter below seafloor) and at Site U1481 sediment was sampled from 1,150 to 1,500 mbsf (Figure 1a, Table S1). The seafloor at these sites lie in waters of 4,147 and 4,178 mbsl (meter below sealevel), respectively. In situ measurements indicate a seafloor temperature of approximately 1.5°C and a geothermal gradient of 44.4°C/km (McNeill, Dugan, Backman, et al., 2017).

The upper 26.4 mbsf sampled at Site U1480 (Unit I) is dominated by fine-grained silicate sand, silt, and clay with varying amounts of calcareous clay and minor biosiliceous components and ash. The 1,225 mbsf sequence assigned to lithologic Unit II at this site reflects the >200 m/Myr quartzo-feldspathic Nicobar Fan deposition that began ∼9 Ma (Figure 1b). The sediments of the fan contain relatively little biogenic debris or volcanic glass and are largely unconsolidated to moderately consolidated although they have local zones of prominent cementation (concretions) (McNeill, Dugan, & Petronotis, 2017).

Within the Nicobar Fan deposits in Site U1480, Subunit IIA (26.4–343.7 mbsf; ∼1.7–3.5 Myr) is a middle- and lower-fan succession characterized by interbedded thin- to medium-bedded, laminated to structureless, fine-grained sand with silty clay and silt. Subunit IIB (343.7–785.8 mbsf; ∼3.5–6 Myr) contains alternating thin- to very thin bedded, cross- and parallel-laminated silt and clay representing a more distal fan environment. The bioturbated black and gray deposits of Subunit IIC (785.8–1,250.3 mbsf; ∼6–9 Myr) contain plant material and mud clasts and have been interpreted as distal-fan deposits. Large, unmineralized (mummified) wood pieces Late Miocene in age, were recovered in this unit (840–860 mbsf) (McNeill et al., 2020). Within Subunit IIC, the sediment is mostly unlithified, but local examples of carbonate-cementation in sandstone and mudstone were encountered. Lithologic Unit III was sampled at both Sites U1480 and U1481. At Site U1480, Subunit IIIA is thought to correspond to the older stratigraphic part of the last active Nicobar Fan, whereas Subunit IIIB is composed of the underlying hemipelagic to pelagic sediment. The volcanogenic-rich sediments of Subunit IIIB contain biosilica (opal) and an amorphous silica phase that originates from almost complete alteration and hydration of volcanic glass, as evidenced from X-ray diffraction analyzes (XRD) and visual observations from smear slides (Hüpers et al., 2017). The diagenetic alteration in this pre-fan succession and its significance for the seismogenic behavior of this subduction zone are described in detail by Hüpers et al. (2017).

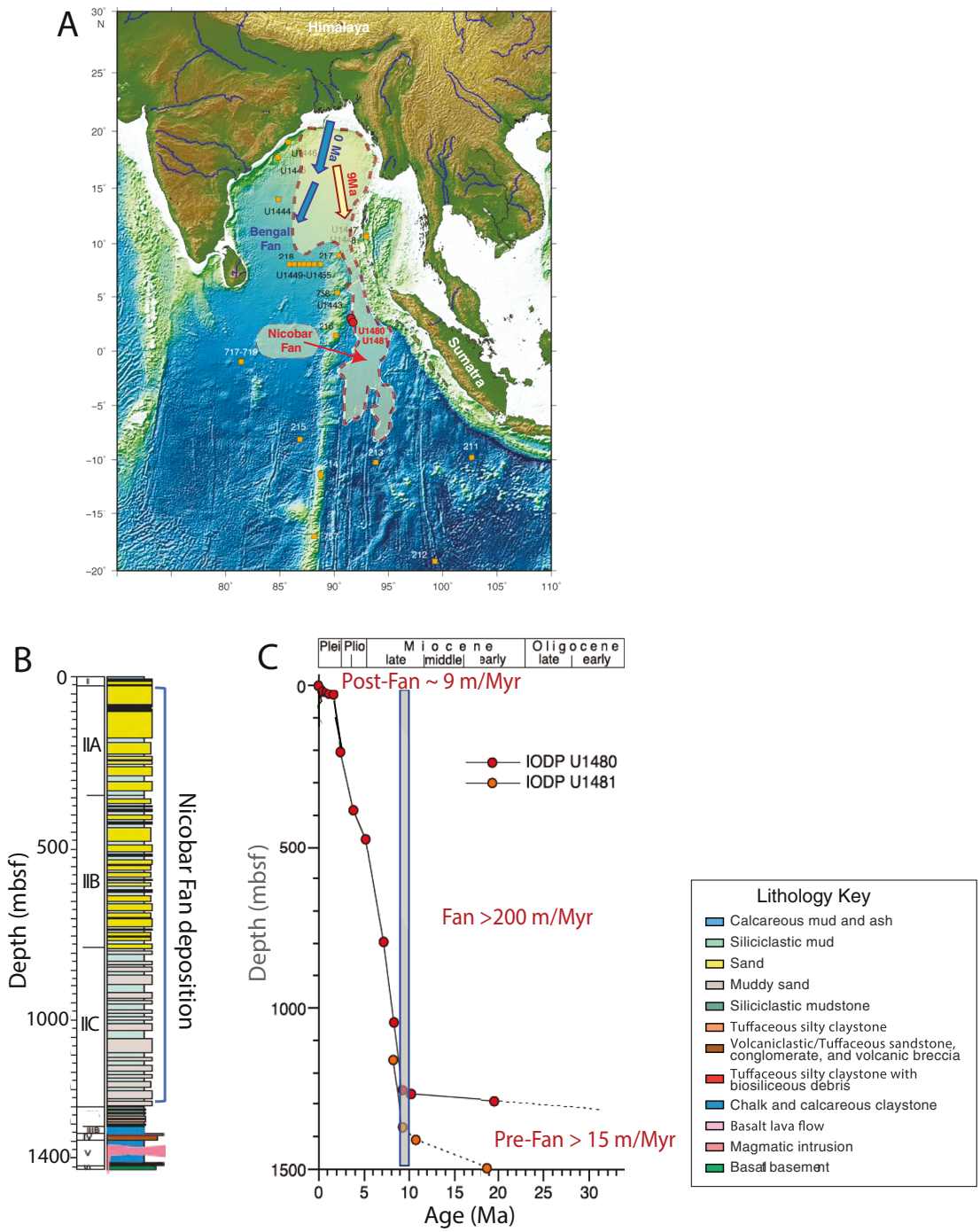

Figure 1. (a) Map of the study area highlighting the evolution of the Nicobar-Bengal Fan as postulated by McNeill, Dugan, Backman, et al. (2017). Sites U1480 and U1481 are demarked by red circles; other sites drilled in this region are denoted by yellow circles. (b) Lithologic column for Site U1480 demarking the units that comprise the Nicobar Fan modified from McNeill, Dugan, and Petronotis (2017). (c) Combined depth versus age curve for Sites U1480 and U1481, indicating the sedimentation rate estimates from McNeill, Dugan, Backman, et al. (2017).

Here we focus on the diagenetic processes that modify the rapidly deposited Nicobar Fan of Lithologic Unit II and the slower phase of early fan deposition of Subunit IIIA (Unit III of Site U1480). Despite proximity to the Sunda forearc, the Nicobar Fan sediments at Sites U1480 and U1481 are almost exclusively continent-derived; the very limited ash content recovered suggests that the Sunda forearc plays a minor role in supplying sediment to these sites. The marked rise in sediment accumulation rate that began 9.5 Ma contrasts with observations at other sites

drilled in the region (McNeill, Dugan, Backman, et al., 2017). This observation, tied to the nature of the siliciclastic sediment deposits originating from the Himalaya, similar in provenance to those recovered from the Bengal Fan, was used by McNeill, Dugan, Backman, et al. (2017) to reconstruct the evolution of the Bengal–Nicobar submarine fan complex in response to tectonic readjustments and climatic change (Figure 1a).

3. Methods

3.1. Pore Fluid and Hydrocarbon Analyses

Pore fluid extraction was conducted onboard, following the procedures described in McNeill, Dugan, and Petronotis (2017). The squeezed pore fluids were collected in pre-cleaned, plastic syringes attached to the squeezing assembly, and subsequently filtered through a 0.45 μm Gelman polysulfone disposable filter. Subsamples collected for strontium isotope analyses were acidified to pH 2 with concentrated ultrapure HNO_3 (Optima grade). Subsamples for the isotopic composition of dissolved inorganic carbon ($\delta^{13}C_{DIC}$) were collected in 2 mL glass vials and preserved with 10 μL of saturated $HgCl_2$.

Methods used to obtain shipboard pore fluid and hydrocarbon concentration data for Sites U1480 and U1481 are detailed in McNeill, Dugan, and Petronotis (2017). Briefly, total alkalinity was determined by Gran titration with an autotitrator (Metrohm 794 Basic Titrino) using 0.1 N HCl at 20°C. Sulfate (SO_4^{2-}) concentrations were analyzed using aliquots of 100 μL diluted 1:100 with deionized water using the Metrohm 850 Professional ion chromatograph (IC). Analytical precision for SO_4^{2-} was better than 2%. Ammonium (NH_4^+) concentrations were determined using an Agilent Technologies Cary Series 100 UV-Vis spectrophotometer following the protocol in Gieskes et al. (1991). The accuracy of the NH_4^+ was better than 2.5%. Calcium (Ca^{2+}), magnesium (Mg^{2+}), strontium (Sr^{2+}), iron (Fe^{3+}) and Mn (Mn^{2+}) were determined onboard using an inductively coupled plasma (ICP) Atomic Emission spectrometer with a Teledyne Prodigy high-dispersion ICP spectrometer after appropriate dilution with ultrapure nitric acid (2%). Analytical precisions for both Ca^{2+} and Mg^{2+} were better than 0.5%, and for Sr^{2+}, Fe^{3+} and Mn^{2+} better than 1% (McNeill, Dugan, & Petronotis, 2017).

For hydrocarbon analysis the headspace vial was heated to 70°C for ∼30 min to evolve hydrocarbon gases from the sediment plug. For gas analysis, 5 cm^3 of headspace gas was extracted from the sealed sample vial using a standard gas-tight syringe and analyzed by an Agilent 7,890 gas chromatograph with a flame ionization detector. The precision is ±2% for concentrations up to 10,000 ppm and ±1% for higher values.

The strontium isotopic data ($^{87}Sr/^{86}Sr$) used in this study was reported by McCarthy et al. (2019). Acidified pore fluid aliquots were loaded directly onto columns containing EICHROM Sr-Spec® resin; samples from the columns were collected in acid-washed teflon bottles, acidified with 2 mL of 3% HNO_3 and analyzed using the Nu Plasma multi collector inductively coupled plasma-mass spectrometer (MC-ICP-MS) located in the W.M. Keck Collaboratory for Plasma Spectrometry at Oregon State University. $^{87}Sr/^{86}Sr$ ratios were normalized to the National Bureau of Standards (NBS) 987 standard, with an $^{87}Sr/^{86}Sr$ value of 0.71025 ± 0.00005 (2σ mean; $n = 91$). External error is represented through replicate analysis of an in-house standard yielded an $^{87}Sr/^{86}Sr$ ratio of 0.70817 ± 0.00005 (2σ mean; $n = 91$).

The stable isotopic composition ($\delta^{13}C_{DIC}$) of the dissolved inorganic carbon (DIC) was measured at Oregon State University using a Gas-Bench II automated sampler interfaced to a gas source stable isotope mass spectrometer as described in Torres et al. (2005). The precision of the $\delta^{13}C$ measurements based on replicate analyses of a $NaHCO_3$ stock solution is better than ±0.1‰.

3.2. Sediment Geochemistry

The carbon and oxygen isotopic composition of carbonate samples was obtained at Oregon State University using a Kiel III device connected to a Thermo Fisher 252 gas source mass spectrometer after a powdered sample was reacted with 100% phosphoric acid at 75°C. Isotopic analyses with this technique yield a precision better than ±0.1 and 0.2% for $\delta^{13}C$ and $\delta^{18}O$, respectively. Isotope data are reported as per mil values in δ notation relative to either the Vienna Peedee Belemnite (V-PDB) standard.

Geochemical analyses of the carbonate samples was obtained by adding a weak buffered acetic acid solution (∼0.33 mol/L acetic acid, ∼0.05 mol/L Na-acetate) to ∼200 mg of dried and powdered sediment and to two

procedural blanks. Samples were rotated for 3 hr on a Labquake Tube Rotator (Thermo Scientific), and the supernatant was decanted into Teflon vials (Savillex). The sample leaches were evaporated to dryness, refluxed with nitric acid to remove organic compounds, and finally redissolved in 1M HCl. A subsample of this leachate solution was used for the strontium isotope analyses (see below), and another subsample was run for elemental composition by external calibration on a Spectro Arcos inductively coupled plasma optical emission spectrometer (ICP-OES) with the torch in Side-On Position. Calibration standards were made from certified primary solutions (Ultra Scientific). Procedural blanks were below the detection limit for all elements.

Dissolved Sr^{2+} in the 1M HCl leachate solution was separated for isotopic analysis using columns containing EICHROM Sr-Spec® resin. $^{87}Sr/^{86}Sr$ ratio was measured using a Neptune Plus MC-ICP-MS (Thermo Fisher Scientific Ltd.) at the Korea Institute of Geoscience and Mineral Resources, Daejeon, Korea. The $^{87}Sr/^{86}Sr$ ratios were corrected for mass fractionation by normalizing to $^{88}Sr/^{86}Sr = 8.375209$ using an exponential function. The ^{85}Rb peak was monitored for interference by ^{87}Rb peaks. The intensity of ^{85}Rb in the sample solution during the Sr isotopic measurements was less than 0.5 mV. Sr isotopic ratios were corrected for this interference assuming $^{87}Rb/^{85}Rb = 0.3857$. Repeated analyses of NBS 987 gave $^{87}Sr/^{86}Sr = 0.71028 \pm 0.00002$ (2σ mean; $n = 19$).

Whole rock geochemistry was obtained by full digestion of powdered squeeze cake samples with HF and subsequent measurement via ICP-OES, at the University of Bremen. Analytical procedures are described in Heinrichs and Herrmann (2013). The amorphous silica data are from Hüpers et al. (2017), who used a 2M KOH sequential extraction procedure followed by dissolved silica spectrophotometric analyses of a silicomolybdate complex.

3.3. Imaging and Petrographic Analysis

Polished thin sections of sediments and lithified sediments were prepared using a vacuum-pressure impregnation technique (Wagner Petrographics). Pores in the sand-size sediments were highlighted with a colored impregnation medium.

Petrographic observations were obtained for all samples using a conventional transmitted, polarizing light microscope. After coating with a thin layer of conductive carbon, additional petrographic observations were obtained using a field emission (FEI) NovaNano scanning electron microscope (SEM) 430. An accelerating voltage of 15 kV and a sample current near the upper end of the instrument range were used. All samples were observed in secondary/back-scattered electron mode and elemental mapping was performed by energy-dispersive spectroscopy using twin Bruker Xflash 30 mm^2 detectors. Maps corresponding to the following elemental mixes were obtained for each mapped areas. Na, Si, Ca; Na, K, Si, Ca; Na, Si, Ca, Fe; Na, Mg, Ca; Na, Mg, K, Ca; and Na, Mg, Ca, Fe. All elemental maps were layered with the secondary/ signal for edge sharpness. The particular elemental mixes chosen highlight major mineralogical components that are common to the grain assemblages of the Himalaya-derived sediments of the Nicobar Fan (quartz, Na-feldspar, K-feldspar, K-, Mg-, and Fe- micas, calcite, dolomite, and K-rich detrital clay minerals). Calcite, dolomite, and siderite that are locally present as authigenic phases are also highlighted by these elemental mixes. The constant false color scheme was employed: Si, red; Na, aqua, Mg, fuschia, K, yellow, Ca, blue, Fe, yellow.

The Na-K-Si-Ca elemental maps were used for point-counting (350 points) of major sandstone components in each of 17 samples. The major goal of the modal analysis is assessment of the compactional state of the sample at the time of cementation through comparison with the observed compaction trend in associated uncemented samples. Thus, detailed categorization of lithic grains was not attempted, rather, the focus of the counting was to determine the ratio of grains to intergrain materials. The major categories counted are monocrystalline quartz, plagioclase, and K-feldspar, lithic grains (mostly plutonic and metamorphic grains), micas (muscovite, biotite, and chlorite), dense minerals, intergranular cements (calcite and Mn-rich Fe-carbonate), detrital clay-size matrix, and intergranular porosity. Carbonate cementation in the concretions tends to be massive and only in one instance (Sample 1481A-32R-3, 98–100 cm; depth 1435.35 mbsf) detectable intergranular pores were counted.

4. Results and Discussion

Concentration data for sulfate, calcium, potassium, strontium, iron and manganese, as well as total alkalinity and methane values can be found in McNeill, Dugan, and Petronotis (2017). Isotopic composition data for dissolved strontium reported in McCarthy et al. (2019), and for dissolved inorganic carbon (this study) are listed in the

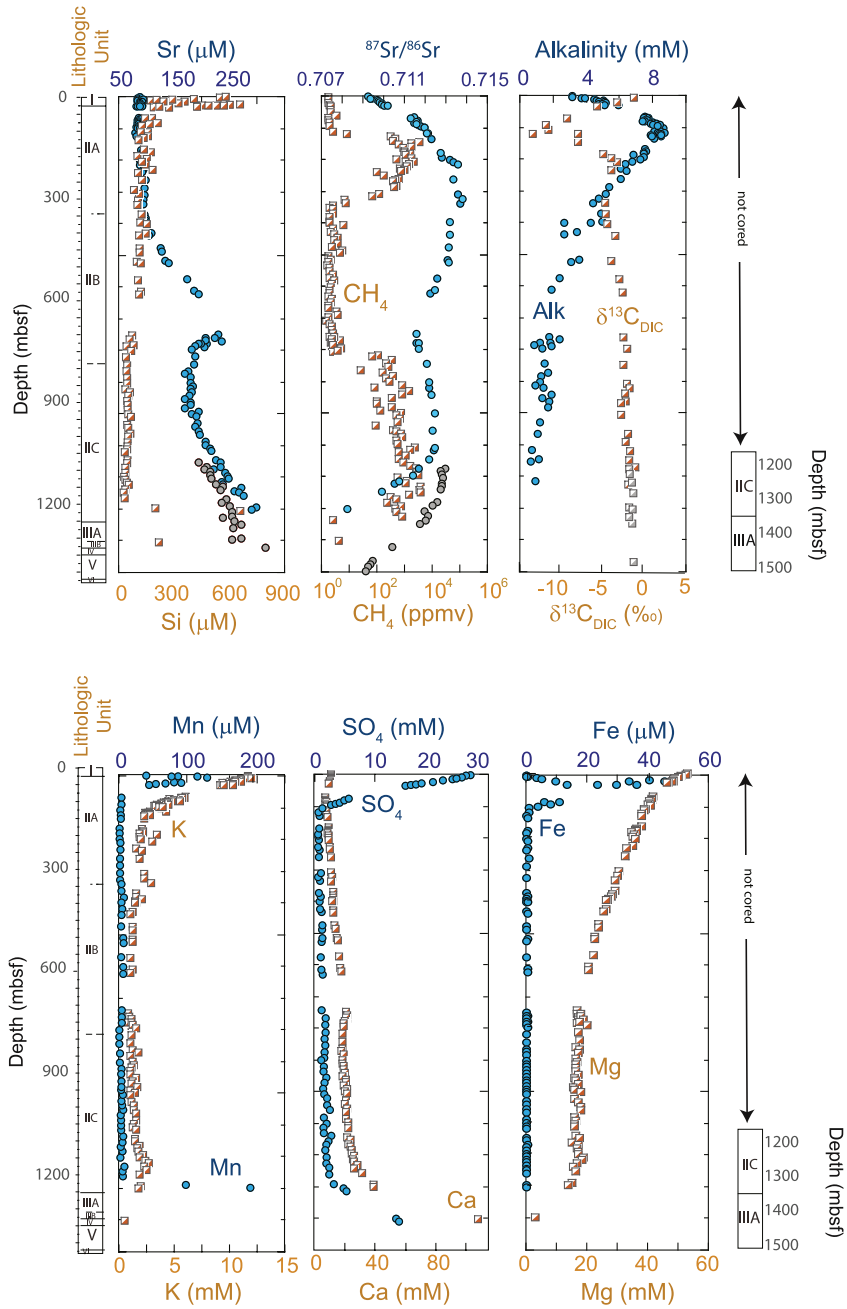

Figure 2. Distribution of dissolved components in the pore fluids and headspace gas in sediments from Sites U1480 (blue circles and orange squares), only the deeper section was sampled in Site U1481 and those data are included as gray symbols. The data gap between 622 and 750 mbsf reflects pore core recovery in this section (<15%), which precluded extraction of interstitial water. Concentration data are from McNeill, Dugan, and Petronotis (2017); strontium isotope data are from McCarthy et al. (2019); dissolved carbon isotope data are from this study and listed in Table S2 (Supporting Information S1).

Supporting Information S1 (Table S2). Pore fluid data are plotted downcore in Figure 2. The data gap between 622 and 750 mbsf reflects poor core recovery in this section (<15%), which precluded extraction of interstitial water. Table S3 lists the carbon and strontium isotope data as well as elemental ratios for the authigenic carbonates. The amorphous silica concentrations, which include both biogenic opal and ash are from Hüpers et al. (2017). Table S4 lists the whole rock geochemical results and chemical index of alteration (CIA) estimates from this study. Point-count data from this study include grain composition parameters and intergranular volume (IGV) estimates for carbonate and siderite concretions are listed in Tables S5 and S6, respectively.

4.1. Biogeochemical and Reactive Silicate Reactions Based on Pore Fluid Data

The uppermost 150 mbsf at Site U1480 have pore fluid profiles that reflect characteristic organic matter remineralization in deep water settings (Figure 2). Sulfate concentrations decrease almost linearly from the seafloor to the sulfate-methane transition zone (SMTZ) at ∼120 mbsf. This relatively deep SMTZ depth is typical for sediments found at depths >3,500 mbsf with low rates of organic carbon accumulation (Egger et al., 2018); this site currently accumulates sediment at rates lower than 15 m/Myr (McNeill, Dugan, & Petronotis, 2017). The concentration of dissolved manganese has a maximum of 131 μM at 6 mbsf, and dissolved iron peaks at 62 μM at 14 mbsf, typical of profiles involving suboxic oxidation of organic matter. Alkalinity increases from a seawater value at the seafloor to a maximum of 8.7 mM, a depth that corresponds to the lowest $\delta^{13}C_{DIC}$ value of −13.2‰, also consistent with remineralization of organic matter of mixed terrestrial and marine sources that characterize the Nicobar Fan sediment deposits (McNeill, Dugan, & Petronotis, 2017). Below the SMTZ depth, alkalinity values gradually decrease with depth to <1 mM in the deepest sections, indicative of strong removal by authigenic carbonate formation.

Below the depth of calcium removal by carbonate precipitation at the SMTZ (∼120 mbsf), there is an increase in dissolved calcium, strontium and manganese toward the base of the sediment section, reflecting supply from alteration of deep volcaniclastics and/or oceanic basement (McNeill, Dugan, & Petronotis, 2017). The increase in dissolved calcium likely supports authigenic carbonate precipitation even at very low alkalinity values (<1 mM) and may be responsible for the carbonate cements observed in lithologic Unit II and in several cores from lithologic Unit III.

Methane content is higher in Subunits IIA and IIC, which correspond to two stages of fan deposition. Subunit IIA shows consistent organic carbon content above 0.6%, reaching in some cases values as high as 1.8%. Subunit IIC contains discrete horizons of woody organic material pointing to local enrichment in terrestrial organic material that accumulate fast enough to fuel methanogenesis (McNeill, Dugan, & Petronotis, 2017, McNeill et al., 2020). In contrast, Subunit IIB represents a more distal fan environment with slightly lower organic carbon content (McNeill, Dugan, & Petronotis, 2017).

4.2. Marine Silicate Weathering

The methane-rich intervals in Subunits IIA and IIC correlate with fluids enriched in ^{87}Sr indicative of alteration of continent-derived silicate minerals, consistent with previous observations that MSiW reactions are facilitated under methanogenesis (see review by Torres et al., 2020, and references therein). Pore fluid data from sediments recovered by drilling from in the eastern Indian margin also document an increase in radiogenic strontium in methane-bearing slope sediment (Solomon et al., 2014). This slope environment received significant input of material derived from erosion of the Himalayas and Tibetan Plateau, with reactive clastic silicates similar in provenance to those in the Nicobar Fan sediments that undergo alteration in anoxic sediment post burial.

Based on the pore fluid analyses shown in Figure 2, we divided the Nicobar Fan sequences into two MSiW zones. MSiW Zone 1, which roughly corresponds to Subunit IIA (24–300 mbsf), is defined by the first marked increase in the $^{87}Sr/^{86}Sr$ ratios (to a maximum value of 0.7114), and a decrease in dissolved silica, calcium and potassium. Overlying this zone, the most recent sediments from lithologic Unit I reflect the pelagic sedimentation that followed rerouting of Himalaya-derived sediment ∼2 Ma from the Nicobar Fan to the Bengal Fan, along the western Indian Ocean (Figure 1a). Underlying MSiW Zone 1, the sediments from lithologic Subunit IIB reflect a transitional zone where MSiW is less intense as evidenced in the $^{87}Sr/^{86}Sr$ data. MSiW Zone 2 (800–1,250 mbsf) corresponds to the second peak in methane and in the $^{87}Sr/^{86}Sr$ ratio (maximum value of 0.71296). This zone encompasses Subunit IIC at Site U1480 and Subunits IIIC and Unit III at Site U1481.

As indicated in Equation 2, authigenic clay formation necessitates a supply of dissolved silica. Extractable silica data at Site U1480, show a decrease from ∼7 wt% at the sediment surface to non-detectable values by 25 mbsf (Figure 3). The decrease in extractable silica in the sediments overlying the Nicobar Fan sequences reflects alteration of the minor ash and biogenic opal components in lithologic Unit I and leads to the rapid increase in dissolved silica from seawater values to 600 μM at ∼10 mbsf. Here, dissolved calcium is mainly supplied from the overlying seawater plus any calcium released from the reactive silicates. This fluid composition contrasts with the early fan deposits in MSiW Zone 2, which receive dissolved calcium from the underlying volcaniclastics and oceanic basement (Hüpers et al., 2017) and lead to calcium concentrations in excess of 100 mM. Alteration of

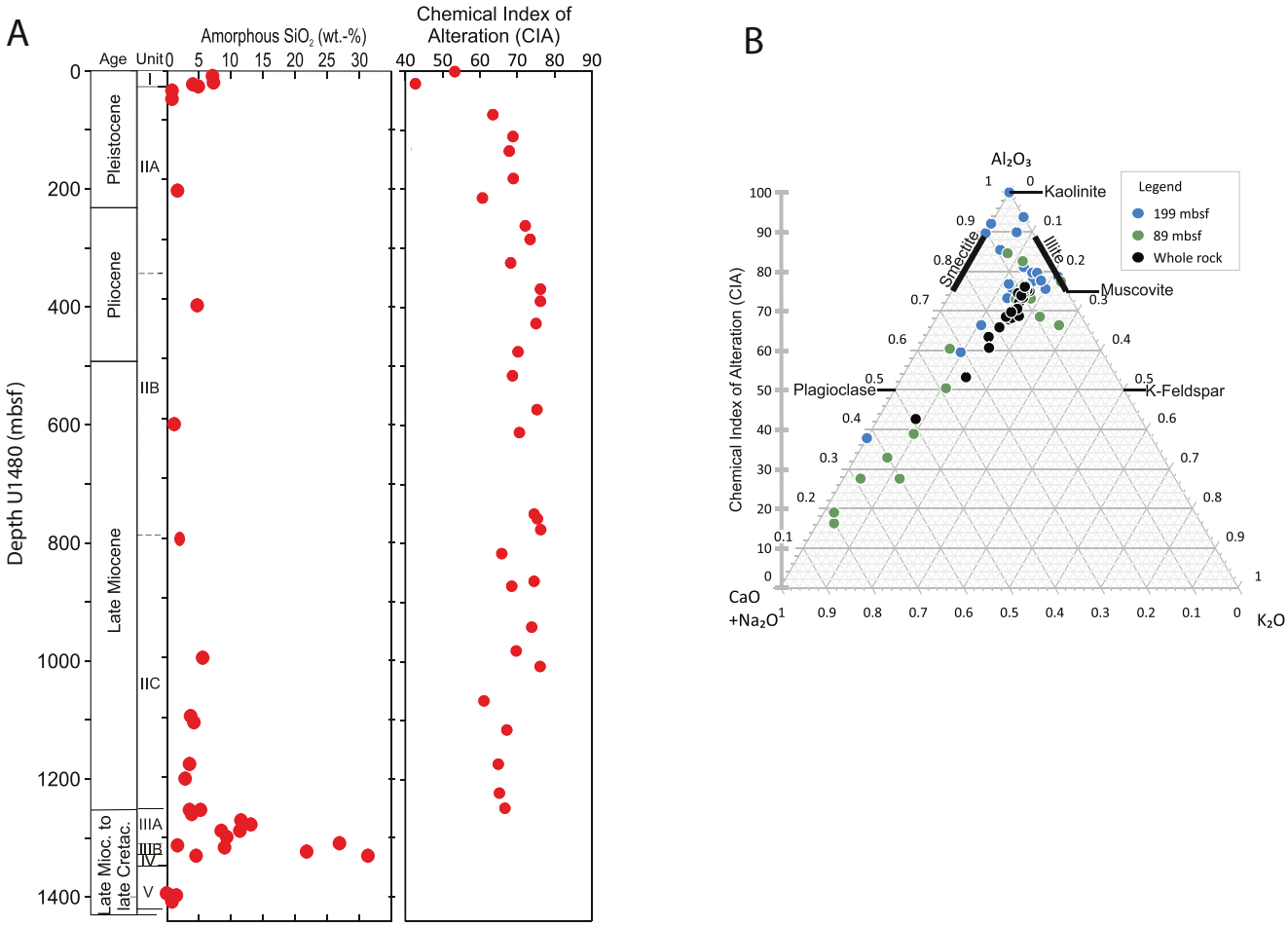

Figure 3. (a) Downcore profiles of amorphous silica content of sediments (data from Hüpers et al., 2017) and chemical index of alteration for Site U1480. (b) Distribution of chemical index of alteration within a ternary diagram indicating sediment composition relative to elemental and theoretical (calculated) mineral components in the sediment (Table S4).

basement basalts and volcanogenic sediments also consumes potassium and magnesium, both cations important in the formation of authigenic clays. The influence of mantle-derived rocks is also reflected in the sharp decrease in the $^{87}Sr/^{86}Sr$ in the pore fluids toward basement, which overprints the contribution of reactive clastic silicates (Figure 2). We suggest that the pore fluid composition in MSiW Zone 2, clearly distinct from that in MSiW Zone 1, is key to promoting precipitation of carbonate minerals, in contrast with the proposed formation of authigenic clays in MSiW Zone 1.

4.3. Geochemical Records in Authigenic Carbonate

Authigenic carbonates formed by MSiW are typically enriched in cations released from alteration of reactive silicate minerals such as Fe, Mn, Mg, and Ba (Equation 1), and can include calcite, dolomite and siderite (Torres et al., 2020). These minerals are distinct from carbonates whose formation was supported by anaerobic oxidation of methane (AOM) at the sulfate-methane transision zone, which are characterized by low $\delta^{13}C$ values that reflect ^{13}C-depleted methane source and are typically high magnesium calcite and aragonite (e.g., Teichert et al., 2014). The methane-derived authigenic carbonates commonly have the strontium isotopic composition of their coeval seawater, in contrast with carbonate minerals formed by alkalinity and cations generated through MSiW, which incorporate the strontium isotopic signal from the reactive silicate being altered (Torres et al., 2020).

The strontium isotopic composition of carbonate samples recovered from both zones is illustrated in Figure 4. MSiW Zone 1 carbonates show smaller deviations in the $^{87}Sr/^{86}Sr$ from coeval seawater (Veizer, 1989), compared

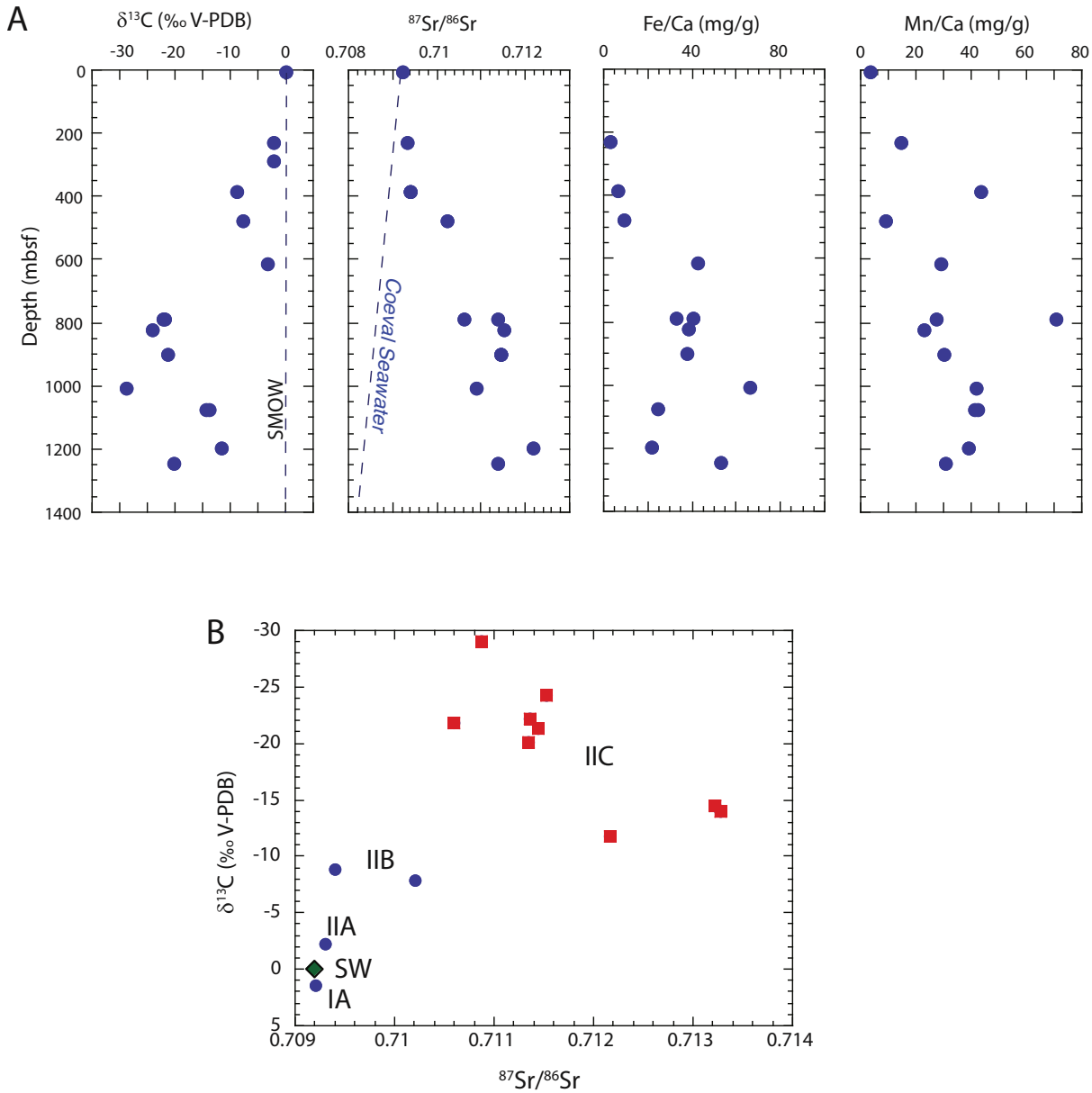

Figure 4. (a) Isotopic and chemical composition of carbonate concretions versus depth. (b) Carbon versus strontium isotopic composition of carbonate concretions. Blue circles represent concretions from Unit II, and red squares denote samples from Unit IIC. Green diamond reflects seawater composition. Data in Table S3.

with the larger deviations recorded in the MSiW Zone 2 carbonate cements. These deep cements are highly enriched in ^{87}Sr, reflecting the radiogenic component of the strontium in pore fluids (Figure 2), and are enriched in Fe and Mn (Figure 4a), consistent with observations of manganoan calcite and siderite in MSiW Zone 2.

At present, the DIC shows a minimum in its carbon isotope signal of −13.2‰ at 117.6 mbsf, and the DIC in deeper fluids has $\delta^{13}C$ values of ca. −1‰ (Table S2). Whereas the carbonate minerals from MSiW Zone 1 show the expected carbon isotope signatures that reflect a mixture of seawater and lightly depleted carbon, the MSiW Zone 2 carbonates have $\delta^{13}C$ values that range from −10 to −30‰, pointing to a contribution of methane-derived carbon remnant from AOM activity at the time of deposition (Figure 4).

Data on fluid and mineral compositional changes with depth point to changes in the processes responsible for authigenic carbonate formation during the burial history, such as documented in samples recovered from the Barkley Canyon (Joseph et al., 2012) and from the sedimentary sequence outboard of the Nankai subduction zone

(Sample et al., 2017). A simple mass balance approach using carbon and strontium isotope data (Table S7) was used to approximate the potential relative contributions of carbonate formed by AOM versus carbonates precipitated by replacement of silicate minerals in MSiW Zone 2, in an approach analogous to that used by Sample et al. (2017). Many assumptions are necessary in constraining these estimates, since we do not have data on the fluid composition that may have precipitated the early carbonate phases during the postulated AOM conditions in the late Miocene. Nonetheless, this simple exercise shows that the strontium and carbon isotope signals in carbonate minerals from MSiW Zone 2 can be explained by a small (<10%) amount of methane derived carbon. Notwithstanding the uncertainties in this estimate, the result is not surprising given the strong carbon fractionation generated by active AOM conditions, but more significantly the carbon isotope data serve to illuminate the prevailing conditions during earlier fan formation. Here strong contribution of organic carbon, probably terrestrially-derived, must have resulted in the development of strong anoxic conditions, with intense methane generation and cycling by anaerobic oxidation.

4.4. Petrography of Authigenic Carbonates and Carbonate-Rich Lithologies

Authigenic carbonate is not uniformly distributed through the sediments and instead displays localization at a range of scales. At larger scales, carbonate precipitation, occurs in concretions, locally pervasive calcite cementation in both sandstone and mudstone (Figure 5). The observed concretions are generally round in form and less than 20 cm across.

Within concretions, minor amounts of both siderite and calcite are localized on the 001 crystal surfaces within expanded micas (Figure 6), a phenomenon that is postulated to be related to favorable pH conditions on the 001 surfaces of these minerals (Boles, 2007; O'Day et al., 1990; Pevear et al., 1990). Most of the siderite, containing variable amounts of Mn, is strongly localized as overgrowths on detrital dolomite (Figures 7a–7c). In contrast, the dominant form of authigenic calcite is broadly distributed, nucleated on all grain types, and filling most of the visible porosity within a given concretion (Figures 7a, 7b, 7d and 8).

Many unstable grains within concretions, for example, Ca-rich plagioclase, dense minerals, and metamorphic lithic grains containing these minerals, are pervasively replaced by the calcite (Figure 8). Siderite is also observed as a grain replacement (Figure 8d). The majority of Na-feldspar and K-feldspar grains do not show extensive dissolution or replacement at the observation scales utilized in this study. This direct grain-scale evidence for a linkage between silicate dissolution and carbonate precipitation (i.e., direct replacement of silicates by carbonate) is seen most dramatically in the deeper, older portions of the Nicobar Fan (Table S5, Figures 7d and 8). Outside the concretions, calcite-replaced grains are not observed and secondary dissolution pores showing a similar magnitude of dissolution are uncommon.

Grain compositional parameters (Tables S5 and S6) are similar in siderite- and calcite-cemented concretions. The average major grain composition is $Q_{55.7}$ $F_{23.1}$ $L_{21.2}$. Mica content averages 4.5% of the whole rock (0.9–11.4); dense minerals average 1.6% (0–3.14). The ratio of feldspar to feldspar + quartz averages 0.30 (0.24–0.35); plagioclase to total feldspar averages 0.66 (0.36–0.89). Compositional grain parameters above display expected variations with grain size (e.g., more mica in finer sand) but do not show systematic trends with depth.

4.5. Intergranular Volume Estimates in Cemented Versus Uncemented Sands

In sand, the IGV at deposition is in the range of 40%–45% (Lundegard, 1992; McBride et al., 1991). In the sediments at the Sumatra drill sites, porosity as measured by the shipboard moisture and density (MAD) method (McNeill, Dugan, & Petronotis, 2017) is a reasonable approximation of the IGV in uncemented sand, because inherited intragranular pores are comparatively rare in siliciclastic sediments. Both MAD and IGV measurements of uncemented sands display a wide range at a given depth due to measurement error and, very likely, sediment sorting, but in general, fall within the range expected for sands in relatively shallow burial (Figure 9). In rigid grain sand, an IGV of around 26% is accepted as the value at compactional stabilization, typically achieved at a depth of 1.5–2.0 km (Paxton et al., 2002). The minimum depth-averaged MAD data for uncemented sand at the Sumatra drill sites falls just above this value in the deepest samples, suggesting that compactional stabilization has not been reached for most samples (Figure 9).

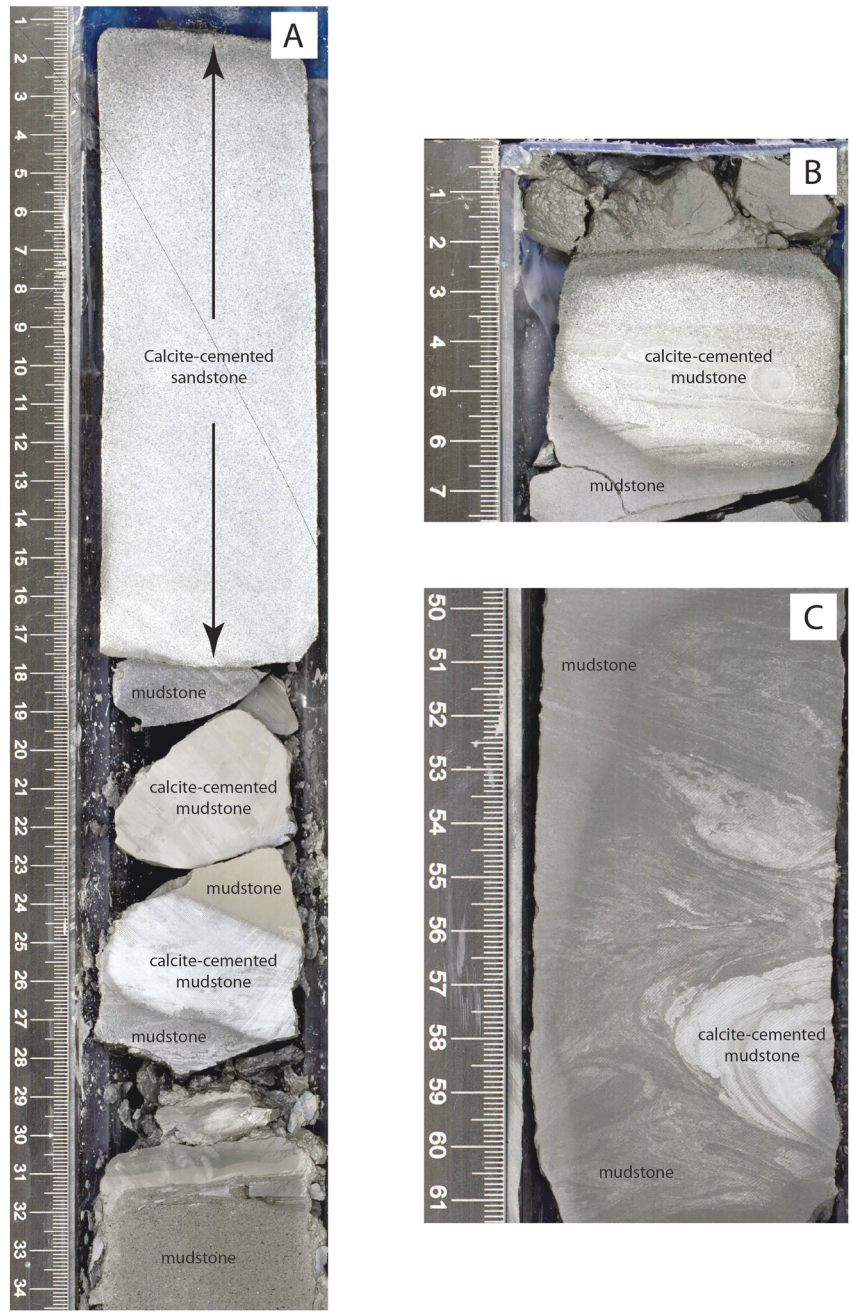

Figure 5. Examples of calcite concretions at the core scale. (a) Both sandstone and mudstone contain localized intervals of cementation (concretions). Core Section 1480F-96X 1, 1–34 cm. (b) Laminations are still clearly visible in the cemented sections of the core. Core Section 1480G-17R 1, 0–7.5 cm. (c) In this interval of soft sediment deformation, the regions of massive (concretionary) and partial cementation partially follow the contorted laminations. The relative timing of deformation and cementation is difficult to resolve, but it is possible that some cementation preceded the early deformation. Core Section 1480G-28R 1, 50–61 cm.

Measured IGVs for cemented samples (Figure 9) fall generally into ranges higher than depth-averaged values for uncemented samples at the same depths, suggesting that cementation has generally occurred at depths less than the present sample depths.

The concretionary sandstone samples analyzed can be divided into two petrographic groups, based on the mineralogy of the authigenic carbonate and the measured IGV. Most cemented samples are calcite-dominated

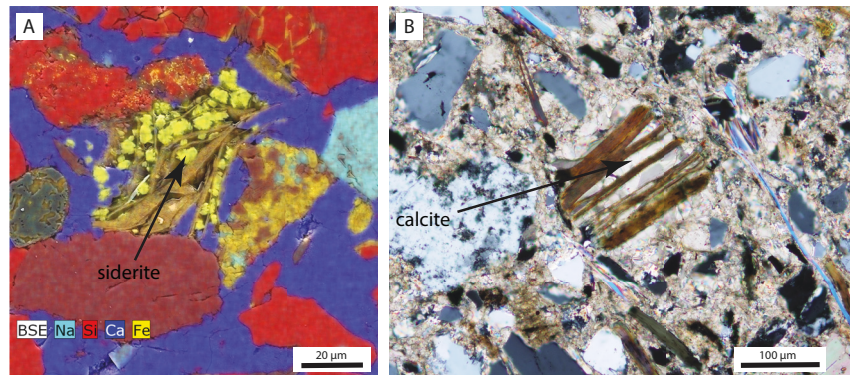

Figure 6. Authigenic carbonate nucleation in micas. (a) Displacive euhedral siderite crystals (bright yellow) nucleated within an expanded Fe-mica. Overall sample is massively calcite-cemented (blue). Sample 1481 A-22R 3, 54–56 cm (depth 1,346.74 mbsf); EDS elemental map (Na, Si, Ca, Fe). (b) Calcite nucleated within an expanded Fe mica. Note that calcite within the mica has larger crystal size than the calcite that fills the intergranular pores. Sample 1480G-53R, 2, 6-4 cm, (depth 1246.14 mbsf); cross-polarized transmitted light image.

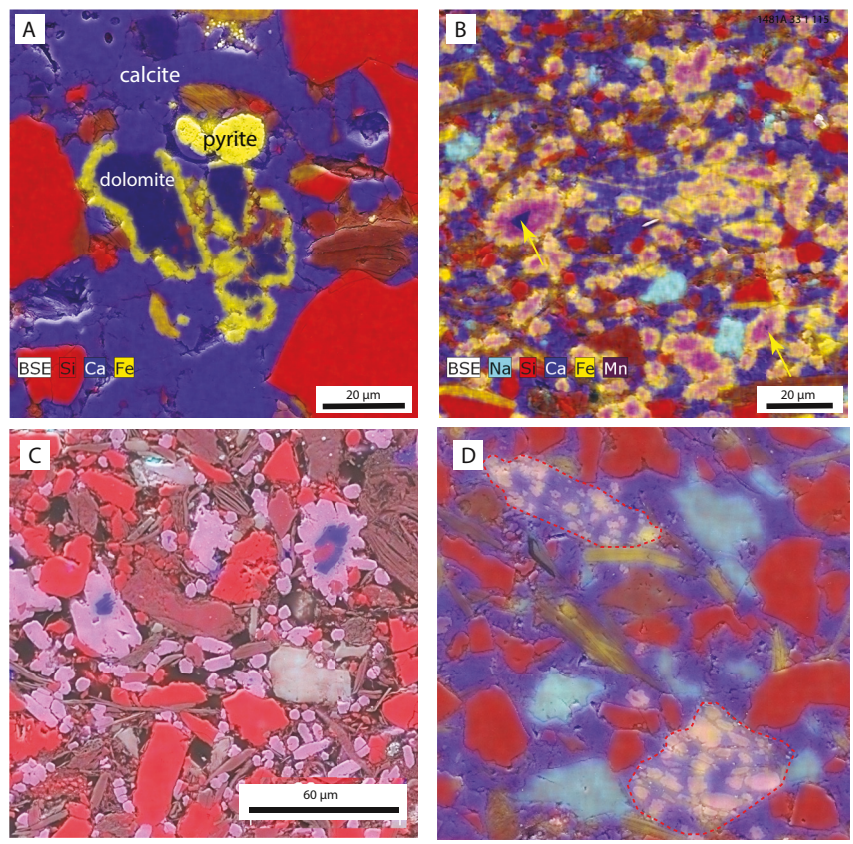

Figure 7. Cementation and replacement in samples containing both Fe-Mn carbonate (pink to yellow, depending on Mn/Fe ratio) and calcite (blue) cements. (a) Microcrystalline rims of siderite (bright yellow surrounding fragments of a polycrystalline detrital dolomite (dark blue). Siderite nucleation in this sample is strongly localized on dolomite and has not occurred on the surfaces of other grains. Overall sample is massively cemented by calcite (blue) that largely post-dates the precipitation of the Fe-carbonate. Sample 1481A-14R 2, 64–66 cm (depth 1268.52 mbsf). EDS elemental map (Si, Ca, Fe). (b) Siderite crystals with Mn-rich interiors (possible rhodochrosite) and Fe-rich rims, nucleated, at least in part, on dolomite grains (dark blue, yellow arrows). Sample 1481A-33R 1, 115–117 cm (depth 1442.55); EDS elemental map (Na, Si, Ca, Fe, Mn). (c) Fe-Mn carbonate in a high-intergranular volume (sample 1481A-33R 1, 115–117 cm, depth 1442.55 mbsf). (d) Unknown grains (approximate edges marked by dashed red lines) have been completely replaced by the two authigenic carbonates (Sample 1481A-33R 1, 78–80 cm; depth 1442.18 mbsf).

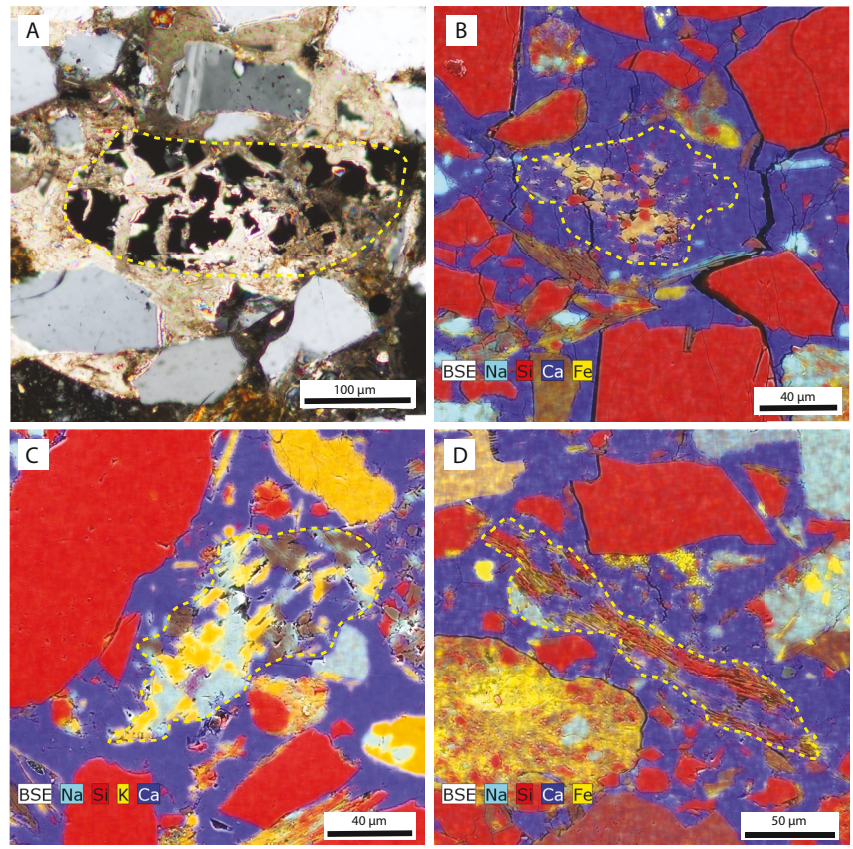

Figure 8. Massive calcite replacement of silicate grains. (a) Plagioclase grain (yellow outline, grain at extinction) extensively replaced with calcite. Sample 1481A-35R 5, 110–112 cm (depth 1476.96 mbsf); cross-polarized transmitted light image. (b) Dense mineral (yellow outline; possible epidote) replaced with calcite (blue). Sample 1481A-22R 3, 54–56 cm (depth 1346.74 mbsf); EDS elemental map (Na, Si, Ca, Fe). (c) Lithic grain (yellow outline) composed of albite (aqua), K-feldspar (yellow), and a dense mineral (gray) with significant calcite replacement (blue). Sample 1481A-22R 3, 54–56 cm (depth 1346.74 mbsf); EDS elemental map (Na, Si, K, Ca). (d) Metamorphic lithic grain composed of mica, quartz, and albite with significant calcite replacement (blue). Sample 1481A-22R 3, 54–56 cm (depth 1346.74 mbsf); EDS elemental map (Na, Si, Ca, Fe).

concretions which have IGVs averaging 36.5% (27%–45%) (Table S5). Only three samples fall into a group containing greater amounts of siderite (Table S6) have higher IGVs (47%–65%), which exceed the 40%–45% IGV expected for sand at deposition (Lundegard, 1992; McBride et al., 1991). The size of individual siderite crystals, especially ones nucleated on dolomite can be large relative to the sizes of expected intergranular spaces.

4.6. Early, Low-Temperature Reaction Products: Authigenic Clay Versus Carbonate

Whereas higher temperature clay formation may be proton-releasing (Abercrombie et al., 1994; Awwiller, 1993; Land et al., 1987; Milliken, 2004), understanding the conditions that result in the precipitation of authigenic carbonates—which sequester carbon—in contrast with those leading to formation of early-formed, low-temperature authigenic clays—which release CO_2—have implications for geochemical budgets of dissolved cations and seawater alkalinity, with significant consequences for the global carbon cycle and the evolution of Earth's climate history.

Here we have documented significant replacement of reactive silicate minerals by authigenic carbonate in the early Nicobar Fan sediments, but note that only a few occurrences of carbonate concretions were recovered from the late fan deposits (stratigraphically higher in the section), and we have shown these shallow concretions to have a smaller contribution of cations from MSiW reactions (Figure 4). Rather, the uptake of silica and potassium in the upper 100 mbsf (Figure 2) point to consumption by formation of authigenic clay minerals (Equation 2).

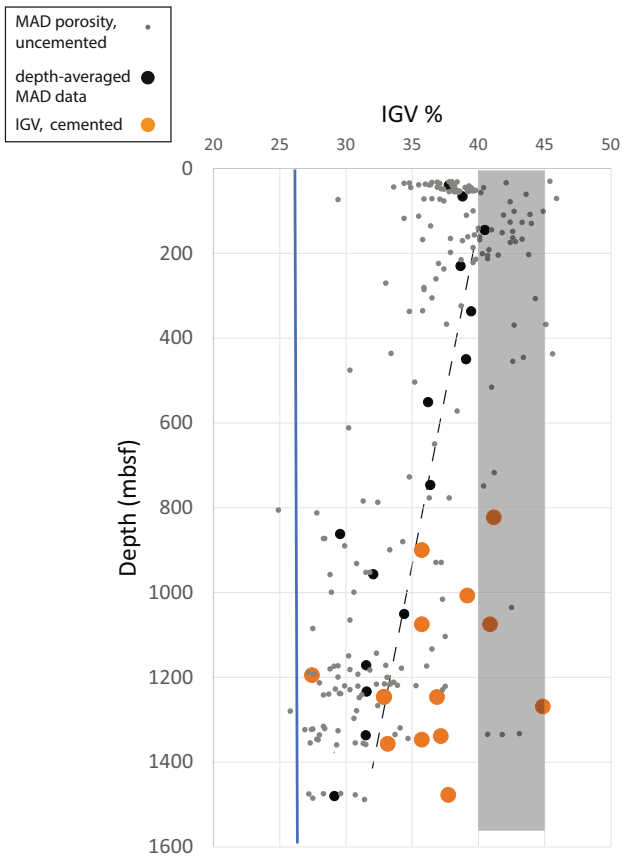

Figure 9. Comparative intergranular volume (IGV) versus depth for cemented and uncemented sands. Shipboard moisture and density (MAD) measurements (gray) are used as an approximation of IGV for uncemented sands, selected for values within the expected range for sands in shallow burial (Lundegard, 1992; McBride et al., 1991; Paxton et al., 2002). Sands with values substantially over 45 percent (likely affected by core disturbance of these unlithified materials) and cemented sands are removed from the MAD data set. Depth-averaged values for MAD values are plotted in black; dashed line is a linear trend through the depth-averaged values. Measured IGV of cemented sands are plotted in orange. Vertical blue line marks the IGV of compactional stabilization in rigid-grain sand (Paxton et al., 2002).

Petrographic data are challenging to obtain in these unlithified sediments to support of our postulate of authigenic clay formation. Careful SEM inspection of mud and sand samples from the later fan failed to locate any petrographic evidence for authigenic clays. Analyses of the <2 μm fraction of the sediment corresponding to MSiW Zone 1 by Rosenberger et al. (2020), document a marked increase in illite (up to 80% of the clay fraction, summing all the illite polytypes), which is interpreted by Rosenberger et al. (2020) as dominantly detrital given the fact that the in situ temperatures are not high enough for illitization of smectite and that most of the illite polytypes are consistent with higher-temperature illite derived from older rocks. A minor amount of the lower-temperature $1M_d$ polytype is described but not quantified. The large primary variations in the ratio of clay minerals to coarser components (silt and sand composed primarily of quartz and feldspar) potentially mask the presence of small amounts of authigenic clays, especially in the dominant mudstones. An alternative sink for the Si would be authigenic zeolites but these were not detected, either petrographically (this study) or by bulk XRD (McNeill, Dugan, & Petronotis, 2017). Authigenic zeolite is most prominently known from volcanogenic sediments (Hay & Sheppard, 2001) and is, thus, not expected as a likely component in the continent-derived sediments of the Nicobar Fan.

We used whole rock chemical analyses of mudstones (Table S3 and Figure 3) to estimate the CIA as defined by Nesbitt and Young (1982), where CIA values of 50 are indicative of unaltered sediments and CIA of 100 indicate completely altered sediment.

$$\mathrm{CIA} = \mathrm{Al_2O_3}/(\mathrm{Al_2O_3} + \mathrm{CaO} + \mathrm{Na_2O} + \mathrm{K_2O}) \quad (3)$$

CIA values for Site U1480 increase from 55 at the seafloor to 72 at 260 mbsf, reflecting the decrease in Na and Ca relative to Al which can be related to some combination of feldspar loss and authigenic clay mineral formation. The observed trend in the whole rock geochemical composition (Figure 3b) points toward an illitic composition for the clay mineral component as also indicated by the results of Rosenberger et al., 2020, who document a dominantly illitic clay mineral assemblage that contains at least a minor fraction of low-T illite ($1M_d$ polytype) which they were unable to quantify. These results point to the likely presence of a K-bearing authigenic clay as an explanation of dissolved potassium uptake. In further support, we note that not all authigenic illite is higher temperature as early-formed illitic clay in weathering environments has been recently documented (e.g., Cuadros et al., 2017; Huggett et al., 2016).

We recognize the potentially diverse source area, depositional, and post-depositional controls on CIA, but argue that our careful selection of uniform mudstone lithology and the relative uniformity of provenance enchance the potential for the CIA to reflect a diagenetic signal. The notable compositional uniformity of sands and muds within the Nicobar Fan (McNeill, Dugan, & Petronotis, 2017; Rosenberger et al., 2020) minimizes the degree of likely provenance change and presents an opportunity to use the fan as a natural laboratory for examining the progression of subsurface processes. At the least, the CIA data show the late fan sediments retain large "reaction potential" for further subsurface weathering. Although the elemental and isotopic composition of the sediment may be controlled by both provenance and diagenesis, the pore fluid data provide indisputable evidence of reactions occurring within the sediment post depositionally. Collectively, these observations, tied to the dissolved strontium isotope data, suggest that in MSiW Zone 1, clay and carbonate are formed as authigenic reaction products from the alteration of detrital silicate. In contrast, the most distinctive feature of MSiW Zone 2 is the presence of carbonate concretions, which are a dominant feature of Subunits IIC and IIIA at Site U1480 and Unit III at Site 1,481 (Figure 5). In both zones, the MSiW reactions appear to be promoted by methanogenesis, as illustrated by the co-occurrence of the enrichment in dissolved radiogenic strontium and methane profiles (Figure 2).

5. Summary and Implications

Regions in SE Asia receive large loads of reactive silicates from rivers in excess of $12{,}500 \times 10^6$ t/year (Milliman & Farnsworth, 2011). MSiW of the cation-rich clastic silicates delivered by Himalayan rivers has been documented as an enrichment in radiogenic ^{87}Sr in pore fluids and solids recovered from the eastern margin of India (Solomon et al., 2014; Torres et al., 2020) and offshore Sumatra (this study).

The depositional environment of the early Nicobar Fan contrasts with present day suboxic conditions that developed ~2 Ma, following rerouting of sediment away from the Nicobar Fan depocenter and toward the Bengal fan. During the later stages of Nicobar Fan deposition (from ~5 to 2 Ma), carbon and strontium isotope data reveals that only a small amount of authigenic carbonate resulted from weathering of the detrital silicate. Rather, based on the observed uptake of dissolved K and Mg, we suggest that MSiW in these sediments result, at least in part, in formation of authigenic clays possibly driven by silica supplied from biogenic opal and ash dissolution in most recent pelagic sediments. In these younger deposits, carbon and strontium isotope data in the recovered carbonates show that only a small fraction of the alkalinity and cations generated by MSiW is sequestered as carbonate minerals.

In contrast, during early deposition of Bengal-Nicobar Fan offshore Sumatra (~9 Ma), MSiW coincided with large Ca flux from underlying oceanic crust, that supported authigenic carbonate formation. Our data reveal that the delivery of reactive detrital silicate minerals and organic material at the onset of fan deposition, led to CO_2 generation by methanogenesis. These conditions promoted in situ subsurface weathering of the silicate minerals, which generated the alkalinity and cations that supported the precipitation of carbonate minerals. Carbon isotopes of these carbonates point to a vigorous carbon cycling environment with significant AOM fueled by methane generation during early fan deposition reflected in the low $\delta^{13}C$ value of these carbonates. Strontium isotope data clearly show the contribution of detrital silicates to the cation pool available for the formation of authigenic carbonates enriched in ^{87}Sr and in Fe, Mn (manganoan siderite and calcite). Petrographic data documenting the occurrence of carbonate-replaced grains solely within the concretions, rules out derivation of replacement via inheritance from older sediments and supports a linkage of silicate dissolution and carbonate precipitation via reaction in Equation 1. As mentioned in the introduction, large impact of diagenesis on both petrographic (McBride, 1987; Milliken, 1988, 1989, 2007; Milliken & Mack, 1990) and geochemical (Milliken et al., 1994; Wilkinson & Haszeldine, 1996) provenance indicators, including the preferential destruction of feldspars via carbonate replacement within concretions, is widely documented in deeply buried sediments. This broader context is fully consistent with the notion that post-depositional MSiW plays a key role in the formation of the concretions recovered in the deeper sediment of the incoming package to the Sumatra subduction zone.

Additional information from the petrographic data is useful in inferring timing and controls on carbonate precipitation, as well as the effect of these cements on the physical properties of the sediment as they enter the subduction zone. The localization of nucleation of authigenic carbonates whether in concretions, at the grain scale in micas, as overgrowths on detrital dolomite, or as grain replacements, suggests strong kinetic limitations on precipitation. For example, the authigenic siderite nucleated as overgrowths on detrital dolomite (Figure 8), follows a style of kinetically-limited heterogeneous nucleation that is similar to that of authigenic quartz in sandstones (Walderhaug, 1996). Such kinetic limitations are consistent with the low-temperatures of carbonate formation and suggest a potential for carbonate supersaturation at the time of precipitation. These conditions are likely to have been present at the onset of fan deposition, as the underlying hemipelagic to pelagic sediment experienced a significant supply of dissolved calcium from alteration of oceanic basement, which even at present reaches concentrations that are ten-fold of seawater values.

The IGV data provide insights on the potential porosity changes associated with carbonate cementation and their associated grain replacements through a direct measure of the compactional state of sediment. The high IGVs of siderite-cemented samples (>45%) are suggestive of displacive cementation, very near the sediment-water interface during early methanogenesis, whereas the calcite concretions have IGV values consistent with the current or somewhat shallower burial depths according to previously documented depth trends for IGV in sand (McBride et al., 1991; Paxton et al., 2002). Again, these IGV results are consistent the idea that carbonate precipitation occurred in the early fan under the influence of elements released into the pore fluids from both the fan sediments and the underlying basement succession.

With regards to the role that MSiW plays on the global carbon budget, it is clear that during methane-rich conditions that prevailed at the onset of Nicobar Fan deposition, alteration of the reactive detrital silicates resulted in carbon sequestration as authigenic carbonate (net CO_2 uptake), most likely in the form of early siderite cement followed by calcite as the rapid sedimentation buried the original deposits to current depths. In contrast, we lack a quantification of the clay and carbonate sink terms during the late Nicobar Fan deposition. Whereas the available fluid composition data suggest formation of authigenic clays with minor carbonate, it is not possible to determine whether MSiW of the most recent fan deposits acted as a source or sink of CO_2.

Data Availability Statement

Data used in this manuscript is available in Milliken et al., 2022 as well as in published cited literature and/or published in the IODP data bases https://zenodo.org/record/3755103#.YcJXiKCIaHs. Shipboard data of JOIDES Resolution are available from the IODP database (http://iodp.tamu.edu/database/).

Acknowledgments
This research used samples and data provided by the International Ocean Discovery Program (IODP). We thank the scientific party, technical staff, and crew of IODP Expedition 362. We thank Jesse Muratli, Andy Ross, Priyanka Periwal and Silvana Pape for assistance in analytical tasks. We gratefully acknowledge the comments from Stan Paxton and from an anonymous reviewer, which improved this manuscript. Milliken and Torres received funding for this research from the U.S. Science Support Program Post Expedition Activity awards and by NSF grant OCE-1833296. AH acknowledges funding through the Deutsche Forschungsgemeinschaft (HU 1789/4-1). JHK received funded by the Korea Ministry of Oceans and Fisheries (NP2011-040).

References

Abercrombie, H. J., Hutcheon, I. E., Bloch, J. D., & De Caritat, P. (1994). Silica activity and the smectite-illite reaction. *Geology*, *22*(6), 539–542. https://doi.org/10.1130/0091-7613(1994)022<0539:saatsi>2.3.co;2

Awwiller, D. N. (1993). Illite/smectite formation and potassium transfer during burial diagenesis of mudrocks. A study from the Texas gulf coast Paleocene-Eocene. *Journal of Sedimentary Petrology*, *63*(3), 501–512. https://doi.org/10.1306/D4267B3B-2B26-11D7-8648000102C1865D

Boles, J. R. (2007). Detrital mica influence on reservoir-scale diagenesis. *Annual Meeting Abstracts, American Association of Petroleum Geologists*, *15*.

Cuadros, J., Andrade, G., Ferreira, T. O., de Moya Partiti, C. S., Cohen, R., & Vidal-Torrado, P. (2017). The mangrove reactor: Fast clay transformation and potassium sink. *Applied Clay Science*, *140*, 50–58. https://doi.org/10.1016/j.clay.2017.01.022

Dunlea, A. G., Murray, R. W., Ramos, D. S., & Higgins, J. A. (2017). Cenozoic global cooling and increased seawater Mg/Ca via reduced reverse weathering. *Nature Communications*, *8*(1), 1–7. https://doi.org/10.1038/s41467-017-00853-5

Egger, M., Riedinger, N., Mogollón, J. M., & Jørgensen, B. B. (2018). Global diffusive fluxes of methane in marine sediments. *Nature Geoscience*, *11*(6), 421–425. https://doi.org/10.1038/s41561-018-0122-8

Gieskes, J. M., Gamo, T., & Brumsack, H. (1991). *Chemical methods for interstitial water analysis aboard JOIDES Resolution*. Ocean Drilling Program, Technical Note 15. https://doi.org/10.2973/odp.tn.15.1991

Hay, R. L., & Sheppard, R. A. (2001). Occurrence of zeolites in sedimentary rocks: An overview. *Reviews in Mineralogy and Geochemistry*, *45*(1), 217–234. https://doi.org/10.2138/rmg.2001.45.6

Heinrichs, H., & Herrmann, A. G. (2013). *Praktikum der analytischen Geochemie*. Springer-Verlag.

Huggett, J., Cuadros, J., Gale, A. S., Wray, D., & Adetunji, J. (2016). Low temperature, authigenic illite and carbonates in a mixed dolomite-clastic lagoonal and pedogenic setting, Spanish central system, Spain. *Applied Clay Science*, *132–133*, 296–312. https://doi.org/10.1016/j.clay.2016.06.016

Hüpers, A., Torres, M. E., Owari, S., McNeill, L. C., Dugan, B., Henstock, T. J., et al. (2017). Release of mineral-bound water prior to subduction tied to shallow seismogenic slip off Sumatra. *Science*, *356*(6340), 841–844. https://doi.org/10.1126/science.aal3429

Hutcheon, I., & Abercrombie, H. (1990). Carbon dioxide in clastic rocks and silicate hydrolysis. *Geology*, *18*, 541–544. https://doi.org/10.1130/0091-7613(1990)018<0541:cdicra>2.3.co;2

Hutcheon, I., Shevalier, M., & Abercrombie, H. J. (1993). pH buffering by metastable mineral-fluid equilibria and the evolution of carbon dioxide fugacity during burial diagenesis. *Geochimica et Cosmochimica Acta*, *57*, 1017–1027. https://doi.org/10.1016/0016-7037(93)90037-w

Joseph, C., Torres, M. E., Martin, R. A., Haley, B. A., Pohlman, J. W., Riedel, M., & Rose, K. (2012). Using the $^{87}Sr/^{86}Sr$ of modern and paleoseep carbonates from northern Cascadia to link modern fluid flow to the past. *Chemical Geology*, *334*, 122–130. https://doi.org/10.1016/j.chemgeo.2012.10.020

Land, L. S., & Macpherson, G. L. (1992). Origin of saline formation waters, Cenozoic section, Gulf of Mexico sedimentary basin. *American Association of Petroleum Geologists Bulletin*, *76*, 1344–1362. https://doi.org/10.1306/bdff89e8-1718-11d7-8645000102c1865d

Land, L. S., Milliken, K. L., & McBride, E. F. (1987). Diagenetic evolution of Cenozoic sandstones, Gulf of Mexico sedimentary basin. *Sedimentary Geology*, *50*, 195–225. https://doi.org/10.1016/0037-0738(87)90033-9

Lu, J., Wilkinson, M., Haszeldine, R. S., & Boyce, A. J. (2011). Carbonate cements in Miller Field of the UK North Sea; a natural analog for mineral trapping in CO_2 geological storage. *Environmental Earth Sciences*, *62*, 507–517. https://doi.org/10.1007/s12665-010-0543-1

Lundegard, D. (1992). Sandstone porosity loss-a 'big picture' view of the importance of compaction. *Journal of Sedimentary Petrology*, *62*, 250–260. https://doi.org/10.1306/d42678d4-2b26-11d7-8648000102c1865d

McBride, E. F. (1987). Diagenesis of the Maxon sandstone (early cretaceous), marathon region, Texas; a diagenetic quartzarenite. *Journal of Sedimentary Petrology*, *37*, 98–107. https://doi.org/10.1306/212f8ab7-2b24-11d7-8648000102c1865d

McBride, E. F., Diggs, T. N., & Wilson, J. C. (1991). Compaction of Wilcox and Carrizo sandstones (Paleocene-Eocene) to 4420 m, Texas Gulf coast. *Journal of Sedimentary Petrology*, *61*, 73–85. https://doi.org/10.1306/d4267690-2b26-11d7-8648000102c1865d

McCarthy, M., Zirkle, B., Torres, M. E., & Haley, B. A. (2019). Data report. $^{87}Sr/^{86}Sr$ in pore fluids from Expedition 362. *Proceedings of the International Ocean Discovery Program*, *362*.

McNeill, L., Dugan, B., Petronotis, K., Milliken, K., & Francis, J. (2020). Late Miocene wood recovered in Bengal–Nicobar submarine fan sediments by IODP Expedition 362. *Scientific Drilling*, *27*, 49–52. https://doi.org/10.5194/sd-27-49-2020

McNeill, L. C., Dugan, B., Backman, J., Pickering, K. T., Pouderoux, H. F., Henstock, T. J., et al. (2017). Understanding Himalayan erosion and the significance of the Nicobar fan. *Earth and Planetary Science Letters*, *475*, 134–142. https://doi.org/10.1016/j.epsl.2017.07.019

McNeill, L. C., Dugan, B., & Petronotis, K. E. (2017). Sumatra subduction zone. *Proceedings of the International Ocean Discovery Program*, *362*.

Milliken, K., Torres, M. E., Hüpers, A., Kim, J.-H., & Lee, S.-G. (2022). *Fluid-rock interaction, Nicobar fan*. Texas Data Repository, V1. https://doi.org/10.18738/T8/AMUHST

Milliken, K. L. (1988). Loss of provenance information through subsurface diagenesis in Plio-Pleistocene sandstones, Gulf of Mexico. *Journal of Sedimentary Petrology*, *58*, 992–1002.

Milliken, K. L. (1989). Petrography and composition of authigenic feldspars, Oligocene frio formation, South Texas. *Journal of Sedimentary Petrology*, *59*, 361–374. https://doi.org/10.1306/212f8f94-2b24-11d7-8648000102c1865d

Milliken, K. L. (2004). Late diagenesis and mass transfer in sandstone-shale sequences. In F. T. Mackenzie (Ed.), *Sediments, diagenesis, and sedimentary rocks. Treatise on geochemistry* (pp. 159–190). Elsevier-Pergamon.

Milliken, K. L. (2007). Provenance and diagenesis of heavy minerals, Cenozoic units of the North-Western Gulf of Mexico sedimentary basin. In M. A. Mange, & D. T. Wright (Eds.), *Heavy minerals in use, developments in sedimentology* (Vol. 58, pp. 47–261).

Milliken, K. L., & Land, L. S. (1991). Reverse weathering, the carbonate-feldspar system, and porosity evolution during burial of sandstones. *American Association of Petroleum Geologists Bulletin*, *75*, 636. https://doi.org/10.1306/0c9b0819-1710-11d7-8645000102c1865d

Milliken, K. L., & Mack, L. E. (1990). Subsurface dissolution of heavy minerals, frio formation sandstones of the ancestral Rio Grande province, South Texas. *Sedimentary Geology*, *68*, 187–199. https://doi.org/10.1016/0037-0738(90)90111-6

Milliken, K. L., Mack, L. E., & Land, L. S. (1994). Elemental mobility in sandstones during burial: Whole-rock chemical data, frio formation, South Texas. *Journal of Sedimentary Research*, *64*(4a), 788–796. https://doi.org/10.1306/d4267ec4-2b26-11d7-8648000102c1865d

Milliman, J. D., & Farnsworth, K. L. (2011). *River discharge to the coastal ocean: A global synthesis*. Cambridge University Press.

Nesbitt, H. W., & Young, G. M. (1982). Early Proterozoic climates and plate motions inferred from major element chemistry of lutites. *Nature*, *299*, 715–717. https://doi.org/10.1038/299715a0

O'Day, A., Pevear, D. R., Zullig, J. J., & Klimentidis, R. E. (1990). Calcite cements in expanded micas suggest bacterial activity. *American Association of Petroleum Geologists Bulletin*, *74*, 732–733. https://doi.org/10.1306/44b4b766-170a-11d7-8645000102c1865d

Paxton, S. T., Szabo, J. O., Adjukiewicz, J. M., & Klimentidis, R. E. (2002). Construction of an intergranular volume compaction curve for evaluating and predicting compaction and porosity loss in rigid-grain sandstone reservoirs. *American Association of Petroleum Geologists Bulletin*, *86*, 2047–2067. https://doi.org/10.1306/61eeddfa-173e-11d7-8645000102c1865d

Pevear, D. R., O'day, A., & Klimentidis, R. E. (1990). Petrogenetic significance of expanded mica fabrics. *American Association of Petroleum Geologists Bulletin*, *74*, 740. https://doi.org/10.1306/44b4b801-170a-11d7-8645000102c1865d

Rosenberger, K., Underwood, M. B., Vrolijk, P., & Haines, S. (2020). Data report: Clay mineral assemblages in hemipelagic sediments entering the Sumatra subduction zone, IODP Sites U1480 and U1481 Expedition 362. *Proceedings of the International Ocean Discovery Program*, *362*. https://doi.org/10.14379/iodp.proc.362.204.2020

Sample, J. C., Torres, M. E., Fisher, A., Hong, W. L., Destrigneville, C., Defliese, W. F., & Tripati, A. E. (2017). Geochemical constraints on the temperature and timing of carbonate formation and lithification in the Nankai Trough, NanTroSEIZE transect. *Geochimica et Cosmochimica Acta*, *198*, 92–114. https://doi.org/10.1016/j.gca.2016.10.013

Smith, J. T., & Ehrenberg, S. N. (1989). Correlation of carbon dioxide abundance with temperature in clastic hydrocarbon reservoirs; relationship to inorganic chemical equilibrium. *Marine and Petroleum Geology*, *6*, 129–135. https://doi.org/10.1016/0264-8172(89)90016-0

Solomon, E. A., Spivack, A. J., Kastner, M., Torres, M. E., & Robertson, G. (2014). Gas hydrate distribution and carbon sequestration through coupled microbial methanogenesis and silicate weathering in the Krishna–Godavari basin, offshore India. *Marine and Petroleum Geology*, *58*, 233–253. https://doi.org/10.1016/j.marpetgeo.2014.08.020

Teichert, B. M. A., Johnson, J. E., Solomon, E. A., Giosan, L., Rose, K., Kocherla, M., et al. (2014). Composition and origin of authigenic carbonates in the Krishna–Godavari and Mahanadi Basins, eastern continental margin of India. *Marine and Petroleum Geology*, *58*, 438–460. https://doi.org/10.1016/j.marpetgeo.2014.08.023

Torres, M. E., Hong, W. L., Solomon, E. A., Milliken, K., Kim, J. H., Sample, J. C., et al. (2020). Silicate weathering in anoxic marine sediment as a requirement for authigenic carbonate burial. *Earth-Science Reviews*, *200*, 102960. https://doi.org/10.1016/j.earscirev.2019.102960

Torres, M. E., Mix, A. C., & Rugh, W. D. (2005). Precise $\delta^{13}C$ analysis of dissolved inorganic carbon in natural waters using automated headspace sampling and continuous-flow mass spectrometry. *Limnology and Oceanography: Methods*, *3*(8), 349–360. https://doi.org/10.4319/lom.2005.3.349

Veizer, J. (1989). Strontium isotopes in seawater through time. *Annual Review of Earth and Planetary Sciences*, *17*, 141–167. https://doi.org/10.1146/annurev.ea.17.050189.001041

Walderhaug, O. (1996). Kinetic modeling of quartz cementation and porosity loss in deeply buried sandstone reservoirs. *American Association of Petroleum Geologists Bulletin*, *80*, 731–745. https://doi.org/10.1306/64ed88a4-1724-11d7-8645000102c1865d

Wilkinson, M., & Haszeldine, R. S. (1996). Aluminium loss during sandstone diagenesis. *Journal of the Geological Society*, *153*, 657–660. https://doi.org/10.1144/gsjgs.153.5.0657